Physics of Plasmas

Azimuthal inhomogeneity of turbulence structure and its impact on intermittent particle transport in linear magnetized plasmas

Cite as: Phys. Plasmas **22**, 112301 (2015); https://doi.org/10.1063/1.4934537
Submitted: 16 July 2015 • Accepted: 11 October 2015 • Published Online: 03 November 2015

T. Kobayashi, S. Inagaki, M. Sasaki, et al.


View Online

Export Citation

CrossMark

ARTICLES YOU MAY BE INTERESTED IN

Structure formation in parallel ion flow and density profiles by cross-ferroic turbulent transport in linear magnetized plasma
Physics of Plasmas **23**, 102311 (2016); https://doi.org/10.1063/1.4965915

Observations of radially elongated particle flux induced by streamer in a linear magnetized plasma
Physics of Plasmas **26**, 042306 (2019); https://doi.org/10.1063/1.5093218

Roles of solitary eddy and splash in drift wave–zonal flow system in a linear magnetized plasma
Physics of Plasmas **26**, 052305 (2019); https://doi.org/10.1063/1.5094577

AIP Publishing

© 2015 AIP Publishing LLC.

Azimuthal inhomogeneity of turbulence structure and its impact on intermittent particle transport in linear magnetized plasmas

T. Kobayashi,[1,a)] S. Inagaki,[2,3] M. Sasaki,[2,3] Y. Kosuga,[2,4] H. Arakawa,[5] T. Yamada,[3,6] Y. Nagashima,[2,3] Y. Miwa,[7] N. Kasuya,[2,3] A. Fujisawa,[2,3] S.-I. Itoh,[2,3] and K. Itoh[1,3]
[1]*National Institute for Fusion Science, Toki 509-5292, Japan*
[2]*Research Institute for Applied Mechanics, Kyushu University, Kasuga 816-8580, Japan*
[3]*Research Center for Plasma Turbulence, Kyushu University, Kasuga 816-8580, Japan*
[4]*Institute for Advanced Study, Kyushu University, Fukuoka 812-8581, Japan*
[5]*Teikyo University, 6-22 Misakimachi, Omuta 836-8505, Japan*
[6]*Faculty of Arts and Science, Kyushu University, Nishi-ku, Fukuoka 819-0395, Japan*
[7]*Interdisciplinary Graduate School of Engineering Sciences, Kyushu University, Kasuga 816-8580, Japan*

(Received 16 July 2015; accepted 11 October 2015; published online 3 November 2015)

Fluctuation component in the turbulence regime is found to be azimuthally localized at a phase of the global coherent modes in a linear magnetized plasma PANTA. Spatial distribution of squared bicoherence is given in the azimuthal cross section as an indicator of nonlinear energy transfer function from the global coherent mode to the turbulence. Squared bicoherence is strong at a phase where the turbulence amplitude is large. As a result of the turbulence localization, time evolution of radial particle flux becomes bursty. Statistical features such as skewness and kurtosis are strongly modified by the localized turbulence component, although contribution to mean particle flux profile is small. © *2015 AIP Publishing LLC*.
[http://dx.doi.org/10.1063/1.4934537]

I. INTRODUCTION

Anomalous transport caused by plasma turbulence has been regarded as a principal obstacle for the realization of a thermonuclear fusion reactor for many years. Nondiffusive and nonlocal properties of plasma transport have been intensely studied since the 1980s,[1] and recently the importance of global structures driven by turbulence, e.g., zonal flows,[2–5] streamers,[6,7] and a long-distance radial correlation modes,[8] has been noted in both experimental and numerical works. These global structures can break the symmetry of turbulence,[9] which is a key factor for explaining nondiffusivity or nonlocality and intermittency of transport. Symmetry breaking in the wavenumber vector domain is also important for generating net momentum transport in the parallel[10] and poloidal[11,12] directions.

In general, recent experiments in basic devices have turned out to be useful for investigating essential physics because these devices have simple geometry, high reproducibility that guarantees good statistics, and multi-point measurement with electrostatic probes. Investigation of zonal flows[13] and streamers[14] has been promoted, along with the direct measurement of symmetry breaking in momentum flux.[15–18] In addition, global structures such as $m = 1$ mode are also intensely studied as a source of intermittent transport of coherent structures, the so-called blobs.[19–24] In particular, the study of initialization of the blob structure, i.e., the shearing-off mechanism of the filament structure, is intensely promoted. For example, the birth of the blob filament is found to be subjected to an elliptical instability of two rotating vortexes in a linear device.[23] Although understanding of nonlinear process in turbulence-structure systems has progressed, direct observation of spatiotemporal dynamics of turbulence that might be affected by the global structure remains challenging. In most cases, turbulence is assumed to be quasi-stationary and spatially homogeneous. Symmetry breaking of otherwise quasi-stationary and homogenous turbulence can lead to a localization of turbulent activity. In this article, we present the turbulence dynamics where that constraint is broken. In a linear magnetized plasma, a turbulence packet that is azimuthally localized at a phase of the global coherent mode is observed. The spatial inhomogeneity is found to be a cause of intermittent particle transport.

This article is organized as follows. In Section II, experimental apparatus are briefly described. Experimental results are presented in Section III. Section IV presents discussion and summary.

II. EXPERIMENTAL APPARATUS

The experiments were conducted in a linear magnetized plasma, Plasma Assembly for Nonlinear Turbulence Analysis (PANTA), which has a cylindrical vacuum chamber with a length of $l = 400$ cm and a diameter of $D = 45$ cm. Background vacuum pressure is 1×10^{-4} Pa before injection of source gas. At one side of the device, Ar plasma is produced with a 3 kW and 7 MHz radio frequency discharge on a double loop antenna.[25] At the other side of the device, the plasma column is terminated with a stainless end-plate. At both sides of the chamber, two baffle plates each of which has an inner diameter of 15 cm are installed in order to maintain the neutral pressure in the confinement region constant.[26] A homogeneous axial magnetic field in the range of $B = 0.03$–0.15 T directed from the source

a)E-mail: kobayashi.tatsuya@LHD.nifs.ac.jp

 © 2015 AIP Publishing LLC

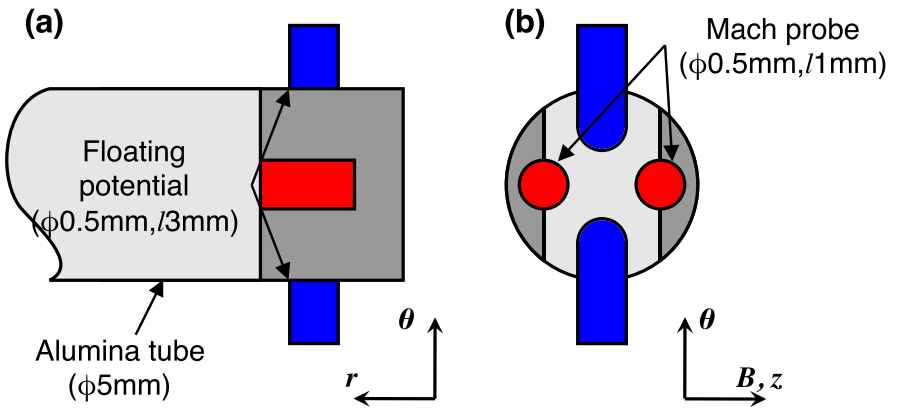

FIG. 1. Schematic view of Mach probe in (a) (r, θ) plane and (b) (θ, z) plane.

region to the end-plate is produced by a set of 18 Helmholtz coils, where z and θ directions of cylindrical coordinates are defined as the magnetic field direction and the right-hand thread direction, respectively. The origin of the z axis is defined as the edge in the source region side of the vacuum chamber. The asymmetry in the axial direction produces a stationary plasma flow structure, depending on the experimental condition. Typical plasma parameters are plasma radius of $a \sim 5\,\mathrm{cm}$, plasma density of $n_e \sim 1 \times 10^{19}\,\mathrm{m}^{-3}$, electron temperature of $T_e \sim 2\,\mathrm{eV}$, and ion temperature of $T_i \sim 0.1 \times T_e$.

In this article, the experimental condition is set to the magnetic field of $B = 0.09\,\mathrm{T}$ and the neutral pressure of $p_n \sim 0.4\,\mathrm{Pa}$ (3.0 mTorr), where the so-called solitary wave type oscillation is routinely observed. The solitary wave is characterized by a sawtooth-like waveform.[27] A dynamic oscillation of nonlinearity was observed by means of the local measurement,[28] which is considered to be a clue for explaining excitation of higher harmonics. By decreasing the neutral pressure, the turbulence regime changes to streamer-type structures.[29,30]

A radially movable Mach probe is installed at $\theta = \pi/4$, $z = 1.625\,\mathrm{m}$, whose probe head can be scanned from $r = 2\,\mathrm{cm}$ $(r/a = 0.4)$ to $r = 6\,\mathrm{cm}$ $(r/a = 1.2)$ on a shot-to-shot basis. The diameter of the probe head is $\sim$5 mm, and the probe head houses four probe tips each of which are 0.5 mm in diameter. The schematic view of the Mach probe is given in Fig. 1. Two tips that are aligned in the azimuthal direction measure floating potential ϕ_f and the azimuthal electric field E_θ can be evaluated as their difference, i.e., $E_\theta = -\Delta\phi_f/d$, where $d = 5.5\,\mathrm{mm}$ denotes the distance between the two tips. The other two tips construct the Mach probe system that measures axial velocity V_z and ion saturation current I_{is} simultaneously. At $z = 2.125\,\mathrm{m}$, a 64-channel azimuthal probe array[31] is installed for determining the azimuthal correlation length and the wavenumber. In the present experiments, I_{is} and ϕ_f are measured with alternative channels at 32 points each. The electron temperature fluctuation is considered to be small, and the floating potential fluctuation and the normalized ion saturation current fluctuation are regarded as space potential fluctuation and normalized density fluctuation, respectively, as $\delta\phi_f \sim \delta\phi$ and $\delta I_{is}/\bar{I}_{is} \sim \delta n_e/\bar{n}_e$. The symbol δ and bar indicate fluctuation and mean variables as $\bar{I}_{is} \equiv \langle I_{is} \rangle$, $\delta I_{is} \equiv I_{is} - \bar{I}_{is}$, where $\langle\rangle$ denotes the long duration average.

III. EXPERIMENTAL RESULTS

Figure 2(a) shows long duration averaged wavelet spectra of the density and potential fluctuations $\delta n_e/n_e$ and $e\delta\phi/T_e$, respectively, at $r = 3\,\mathrm{cm}$ $(r/a = 0.6)$. For comparison, the Fourier spectrum of density fluctuation is also plotted. The

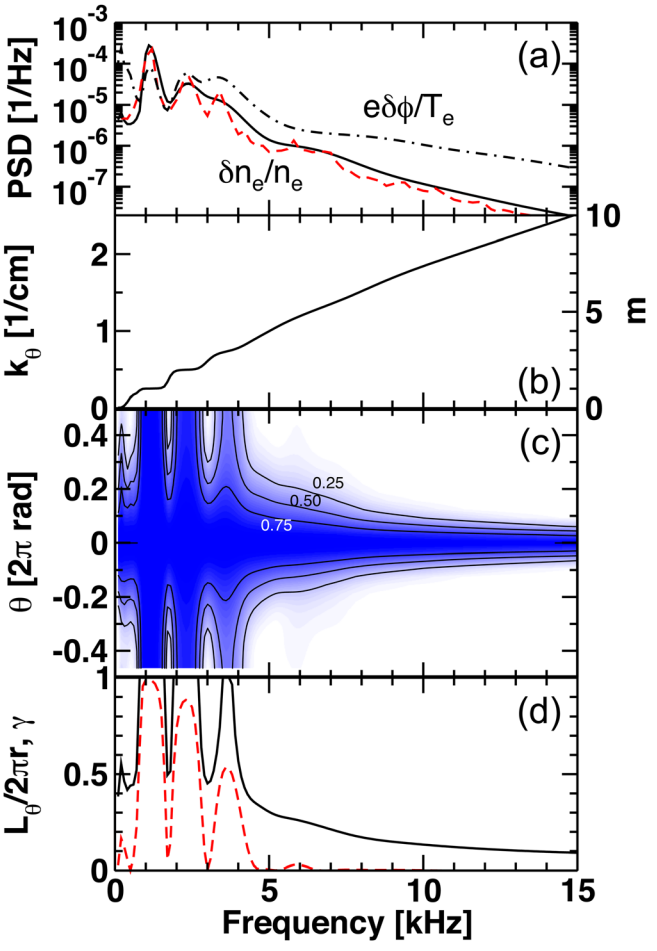

FIG. 2. (a) Long duration averaged Wavelet power spectrum of normalized density (black solid) and floating potential (black dashed-dotted) fluctuation at $r = 3\,\mathrm{cm}$. Red dashed curve shows Fourier power spectrum of normalized density fluctuation. (b) Azimuthal wave number and corresponding azimuthal mode number, shown with the left and right vertical axes, respectively. (c) Azimuthal distribution of squared cross coherence of density fluctuation computed with the reference channel at $\theta = 0$. (d) Correlation length (black solid) and squared cross coherence at $\theta = \pi$, the farthest point from the reference (red dashed).

Fourier spectrum has more discrete spectral peaks because of its finer frequency resolution in the high frequency regime. Azimuthal wave number k_θ and corresponding mode number m of the density fluctuation are given in Fig. 2(b), which is calculated with phase difference of the azimuthal probe array signals at $r = 4$ cm. The density and potential power spectra are dominated mainly by the fundamental mode at $f = 1.1$ kHz that has $m = 1$ structure. There also are the second and third harmonics, at $f = 2.2$ kHz ($m = 2$) and $f = 3.3$ kHz ($m = 3$), respectively. The fundamental mode and two harmonics are coherent, and most of the fluctuation power is occupied by these three modes. The power fractions between the density and potential fluctuations are different at each spectral peak. Above the third harmonic, the shape of the spectral curves changes to a rather turbulent-like shape. The wavenumber spectrum becomes almost a straight line, though it is shaped like a staircase for the first three coherent modes. In the laboratory frame, fluctuations at each frequency propagate in the electron diamagnetic direction at almost the identical speed of ~300 m/s, which means that the phase locking occurs. The mechanism of the phase locking can be explained though nonlinear energy transfer from a linearly unstable mode to either larger-scale[32] or smaller-scale[33] fluctuations. Once the phase locking occurs, depending upon the relative phase of the higher harmonics with respect to the fundamental mode, long-lived steepening of the azimuthal gradient, sometimes called a "shock front," can be seen. There are two types of the shock front: the wave with a shock front at the front and the wave with a shock front at the back in the wave propagation direction. For the case of the drift wave turbulence, the selection rule of the shock front is given,[33] where the authors remarked that the sign of the parameter $\partial_r \ln[|e\delta\phi/T_e|/|\delta n_e/n_e|]$ showing the violation of the Boltzmann relation determines the shock front. Figure 2(c) illustrates the azimuthal distribution of squared cross coherence of the density fluctuation where the reference channel is taken at $\theta = 0$. From Fig. 2(c), azimuthal correlation length is computed as the full width at half maximum, as shown in Fig. 2(d). Azimuthal correlation length also shows clear transition at the frequency of $f = 4$ kHz, which is the boundary frequency of the third harmonic. Below $f = 4$ kHz, the correlation length far exceeds the length of the circumference at the peaks of the power spectrum. In Fig. 2(d), the value of squared cross coherence γ^2 at the farthest point from the reference is also plotted. At the fundamental mode frequency, γ^2 is still very close to unity, corresponding its long correlation length. For higher harmonics, γ^2 decreases. Above $f > 4$ kHz, the correlation length drops less than the half-length of the circumference and decreases together with the frequency. The typical ratio of correlation length and azimuthal wavelength, $L_\theta/\lambda_\theta \equiv mL_\theta/2\pi r$, is of the order of unity for that regime. We define the fluctuation component below (above) $f = 4$ kHz coherent (turbulence) regime.

From numerical analysis in the cylindrical low temperature plasma similar to PANTA, linear excitation energy is known to focus on a small number of low m coherent modes, which are responsible for further nonlinear evolution.[29,33] As will be shown below in Fig. 5, the fluctuations in the coherent regime have the intermittent inward particle pinch at the location where the axial velocity shear is largest, in contrast to the feature of linearly unstable drift wave. Parallel Reynolds stress $\langle \delta v_r \delta v_z \rangle$, where δv_r and δv_z are the radial and axial velocity fluctuations, respectively, is directly measured and the mode is found to extract free energy from the radial shear of axial velocity and not from the density gradient. The instability, therefore, can be a Kelvin-Helmholtz type instability driven by an axial velocity gradient, the so-called D'Angelo mode, as has been discussed in Refs. 18 and 34. Indeed, the necessary condition of the D'Angelo mode, $k_z k_\theta v_z' > 0$, where k_z, k_θ, and v_z' are the axial wavenumber, the azimuthal wavenumber, and the radial shear of the axial flow velocity, respectively, is found to be satisfied (i.e., $k_z \neq 0$). Note that the link between the inward particle pinch and (azimuthal) velocity shear driven instability is investigated elsewhere.[21,24] This kind of global mode can also be generated by the nonlinear energy transfer from smaller scale modes to $m = 1$ mode, as shown in Ref. 32.

Because the propagation velocity of the fluctuations is almost identical, lock-in averaged time evolution with respect to the phase of the fundamental mode (see the Appendix for the definition) can be transferred to the azimuthal distribution by replacing the variables ($t \rightarrow -\theta$). Using data from the radially movable probe, the radial profile of the lock-in averaged time evolution $\bar{x}(r, \theta)$ can be obtained, where the phase of the waveform at each radius is fixed at a certain point. At the same time, the radial profile of the mean relative phase of the fundamental mode $\psi(r)$ can be calculated with a reference probe. Here, the tip of the azimuthal probe array at $\theta = \pi/4$ measuring the density fluctuation is used for the reference. Note that the value of the squared cross coherence between the reference probe and the radially movable probe is always close to unity for the fundamental mode. In addition, since cross coherence among signals from the azimuthal probe array tips is almost unity for the fundamental mode, the relative phase of the fundamental mode in the different radii does not rely on the choice of the reference tip. The two-dimensional wave pattern of the measured variables can be reconstructed by compensating the initial phase as $\bar{x}(r, \theta + \psi(r))$. Figures 3(a) and 3(b) exhibit the reconstructed wave pattern for the normalized density fluctuation and the potential fluctuation, respectively. The normalized density fluctuation has a quasi-positive-to-negative symmetry. Modes propagate radially outward as they rotate in the electron diamagnetic direction. In contrast, the potential perturbation has a standing wave-like structure. By taking a spatial high pass filter having a cut-off between $m = 3$ and 4, turbulence components of the fluctuations are extracted, as displayed in Figs. 3(c) and 3(d) for the normalized density fluctuation and the potential fluctuations, respectively. The density and potential turbulence components are azimuthally localized at the fourth quadrant. The wave pattern shows a spiral shape, where the phase at the outer radius is delayed, along with the waveform of the normalized density fluctuation [see Fig. 3(a)]. Both turbulent density and potential structures propagate preferentially outward. The turbulent density field exhibits a finer structure than the potential field. In contrast to the case of azimuthal direction, turbulent density and potential maintain their correlation in

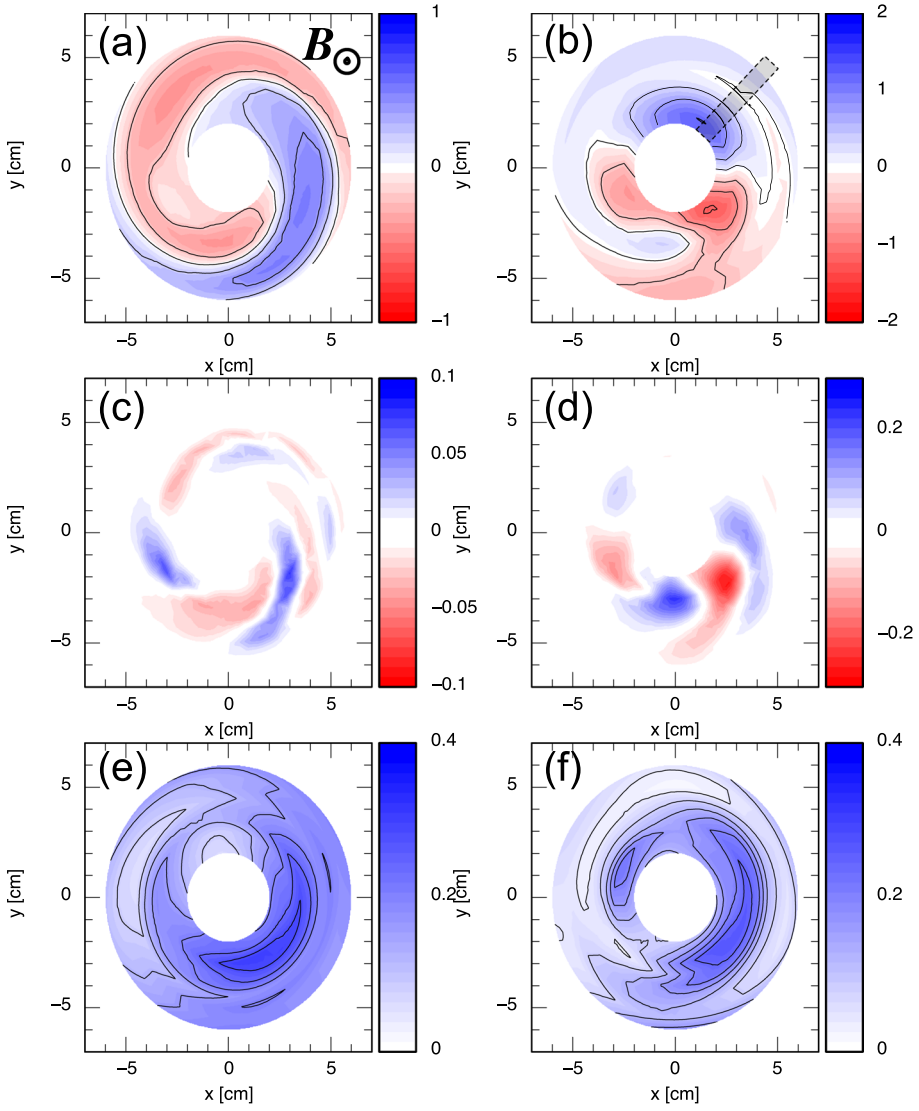

FIG. 3. Conditional averaged wave pattern of (a) density and (b) potential fluctuation in the azimuthal cross section, and their turbulence component [(c) and (d), respectively]. Summed bicoherence with respect to (e) the fundamental mode, $f_3 = 1.1 \pm 0.4$ kHz and (f) the second harmonic, $f_3 = 2.2 \pm 0.4$ kHz. Shaded rectangle in (b) shows the position of the radially movable probe and the reference tip of the azimuthal probe array for this analysis.

the radial direction. As has been discussed above, the large scale coherent fluctuations are considered to be linearly unstable. Therefore, we assume that the turbulence components are nonlinearly excited by the modes in the coherent regime. Conditional averaged summed squared bicoherence is computed using Eq. (A4) (see Appendix). The phase of the reference signal is divided into $M = 8$ sections where squared bicoherence is calculated in each section, respectively, and then the two-dimensional pattern is reconstructed with the mean relative phase of the fundamental mode $\psi(r)$. Figures 3(e) and 3(f) show summed squared bicoherence of the potential fluctuation with respect to the fundamental mode $f_3 = 1.1 \pm 0.4$ kHz and the second harmonic $f_3 = 2.2 \pm 0.4$ kHz, respectively. Here, f_1 for the summed squared bicoherence is taken from the turbulence regime, i.e., $f_1 > 4$ kHz, where f_2 is automatically determined from the matching condition $f_2 = f_3 - f_1$. Because the turbulence components are linearly stable, the value of the summed squared bicoherence can be an indicator of the strength of nonlinear energy transfer from the coherent modes to the turbulence. Summed squared bicoherence is high at the fourth quadrant, where the high frequency turbulence components have large amplitude. The nonlinear interacting region is mainly restricted to the large amplitude region of the coherent modes.

In the next step, the effect of the inhomogeneous bunching of the turbulence on the particle transport is studied. Instantaneous fluctuation-driven radial particle flux is defined as

$$\Gamma_r = \delta n_e \delta E_\theta / B \tag{1}$$

and is routinely calculated with the radially movable probe. Figure 4(a) shows the typical time evolution of the local particle flux normalized by the electron density, i.e., equivalent radial mass flow velocity. Positive Γ_r corresponds to radially outward particle flux. In the time evolution, intermittent bursts of inward particle flux often appear, and the long duration averaged particle flux seems to be negative. Note that the ratio between the mean axial velocity and the equivalent radial flow velocity v_z/v_r is in the order of 10 (Fig. 5), thus the flow vector is dominated by the axial flow. However, a typical length of the plasma column L is 100 times longer than the plasma radius a. Considering effective particle confinement time in the axial direction $\tau_z \equiv L/v_z$ and the radial direction $\tau_r \equiv a/v_r$, $\tau_z = 10\tau_r$ holds. Therefore, the radial particle flux is essential for the plasma confinement. The lock-in

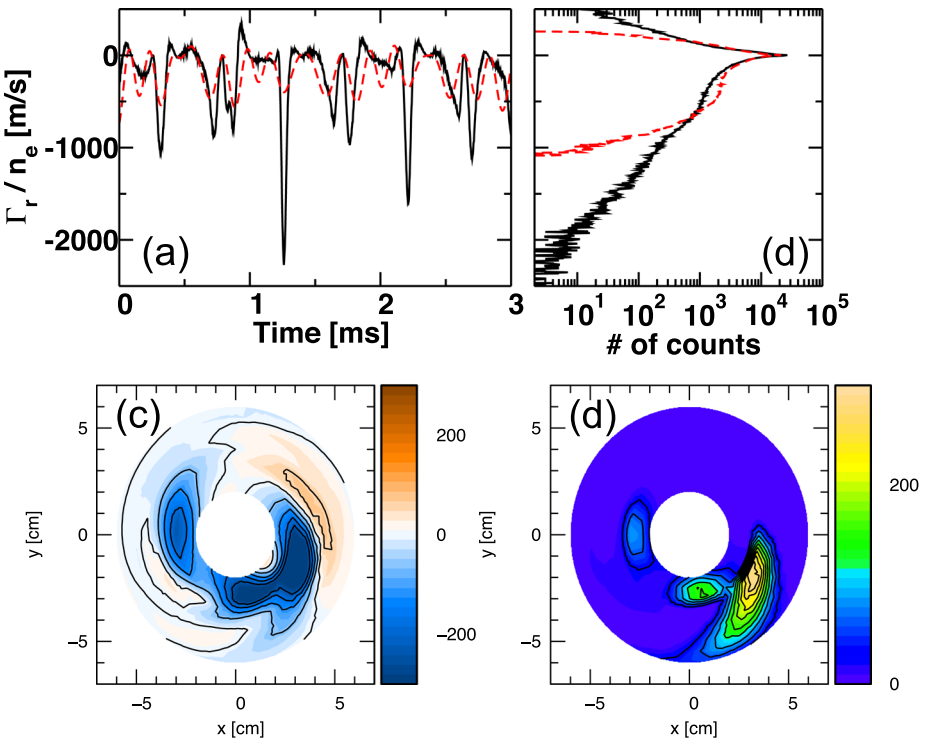

FIG. 4. (a) Time evolution of the total particle flux (black solid) and the particle flux driven by the coherent modes (red dashed), normalized by the electron density. (b) Probability distribution function of normalized local particle flux. (c) Conditional averaged wave pattern of normalized particle flux. (d) Probability distribution function of occurrence phase of normalized particle flux burst.

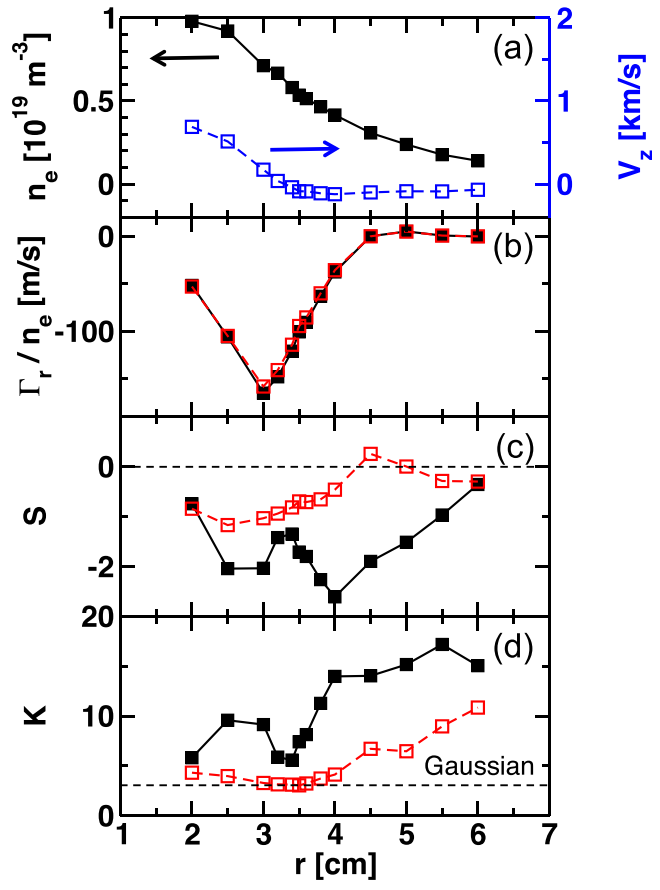

FIG. 5. Radial profile of (a) mean density and axial velocity, (b) normalized local particle flux, (c) skewness S, and (d) kurtosis K of particle flux. Black closed square and red open square show the profile for total particle flux and particle flux driven by coherent modes, respectively.

average two-dimensional wave pattern of the particle flux corresponding to Fig. 3 is shown in Fig. 4(c), although the intermittent feature of the particle flux is averaged out. On the cross section, strong inward pinch is seen at the fourth quadrant, inner radii, where the turbulence amplitude is also large. In addition, at $y=0$ cm, $x=3$ cm, another isolated peak is found. Basically, periodic rise and fall of the inward flux is observed at a fixed local point as the pattern rotates.

In order to examine the effect of the inhomogeneous turbulence bunching on particle transport, terms in Eq. (1) are expanded as $\delta n_e = \hat{n}_e + \tilde{n}_e$ and $\delta E_\theta = \hat{E}_\theta + \tilde{E}_\theta$, where hat and tilde indicate the fluctuation component in the coherent regime ($f<4$ kHz) and the turbulence regime ($f>4$ kHz), respectively. Equation (1) becomes

$$\Gamma_r = [\hat{n}_e\hat{E}_\theta + \tilde{n}_e\tilde{E}_\theta + \hat{n}_e\tilde{E}_\theta + \tilde{n}_e\hat{E}_\theta]/B. \qquad (2)$$

The third and fourth terms in the right-hand-side (RHS) have no contribution to mean particle flux because they are products of two terms having exclusive frequency ranges. First, we compare the total flux Γ_r with the first term of the RHS, which we call coherent particle flux $\Gamma_{r,\mathrm{coh}}$. In Fig. 4(a), the red dashed curve plots the time evolution of $\Gamma_{r,\mathrm{coh}}/n_e$. In contrast to the time evolution of Γ_r/n_e, inward flux bursts disappear. However, if one takes a long duration average, both particle fluxes provide almost identical values. The turbulence component provides no substantial impact on the mean particle flux, because its amplitude is far below that of the coherent component. Nevertheless, the localized turbulence components are essential for the intermittent property of the transport, which is well described in Fig. 4(b), the probability distribution function (PDF) of Γ_r/n_e and $\Gamma_{r,\mathrm{coh}}/n_e$. The PDF of the total particle flux exhibits a large negative tail, which becomes much smaller if one neglects the turbulence

components. As shown in Fig. 4(a), inward flux bursts occur when the coherent particle flux reaches its negative temporal peak. In order to obtain a more complete picture of the correlation pattern, the radial profiles of the PDF of the peak location of inward flux bursts have been calculated. Here, we only take the inward flux peaks that have an amplitude larger than $\bar{\Gamma}_r + 3\sigma$, where $\bar{\Gamma}_r$ and σ denote mean value and standard deviation of the time series, respectively. Figure 4(d) depicts the PDF of bursty events showing overall good agreement with the conditional averaged particle flux [Fig. 4(c)]. The PDF of bursty events also has a correlation with the amplitude of turbulence modes, as shown in Figs. 3(c) and 3(d), which implies that the intermittent flux burst is driven by the turbulence components.

Figure 5 plots the radial profile of mean and statistical features of the radial particle flux. Mean electron density and axial velocity profiles are shown in Fig. 5(a). Both profiles have a maximal gradient at $r \sim 3$ cm. The mean particle flux normalized by the electron density is given in Fig. 5(b) for the total particle flux (black closed square) and the coherent particle flux (red open square). As discussed above, the coherent particle flux dominates the total flux and the contribution due to the turbulence components is negligibly small. Figures 5(c) and 5(d) show skewness S and kurtosis K, which are the third and fourth moments of the time series. A large negative skewness indicates more negative than positive spikes in a time series leading to negative tails in the PDF. The kurtosis is thought to measure both the "peakedness" of the distribution and the "heaviness" of its tail. Non-intermittent Gaussian statistics correspond to $K = 3$. Neglecting the turbulent component, the skewness of the coherent particle flux is one-half of the total flux at $r \sim 3$ cm, exactly where the mean particle flux exhibits its maximum. The skewness of the total flux takes the maximum at $r \sim 4$ cm and decreases with radius at $r \leq 4$ cm. The kurtosis exceeds $K \gg 3$ at each radius indicating an extremely spiky total flux. Both S and K exhibit a local minimum around $r \sim 3.5$ cm. Without the turbulent component K approaches to 3 at $r \leq 4$ cm, which corresponds to a Gaussian-like coherent particle flux. At $r > 4$, S becomes almost zero and K increases with r. The particle flux caused by the coherent modes also changes the feature from inward-preferential non-intermittent transport to non-preferential intermittent transport. Although the impact on the mean particle flux is negligibly small, drastic changes to the statistical features are brought by the fluctuations in the turbulence regime.

Next, the possible agent leading to the intermittent total flux is investigated in more detail. Lock-in average of each term in Eq. (2) is computed using a different trigger, the peak of the inward total particle flux larger than $\bar{\Gamma}_r + 3\sigma$. Figure 6(a) shows the lock-in average time evolution of the first term (the coherent particle flux $\Gamma_{r,\mathrm{coh}}$) and the third term of the RHS in Eq. (2), as well as the total particle flux Γ_r, where the values are normalized with the electron density n_e. We call the third term transient particle flux, $\Gamma_{r,\mathrm{trans}}$. The impact of the other two terms in RHS on the total particle flux is negligibly small. Note that the fraction between the third term and the fourth term is $(\tilde{E}_\theta/\hat{E}_\theta)/(\tilde{n}_\mathrm{e}/\hat{n}_\mathrm{e})$. Figure 2(a) indicates the ratio between the density and potential

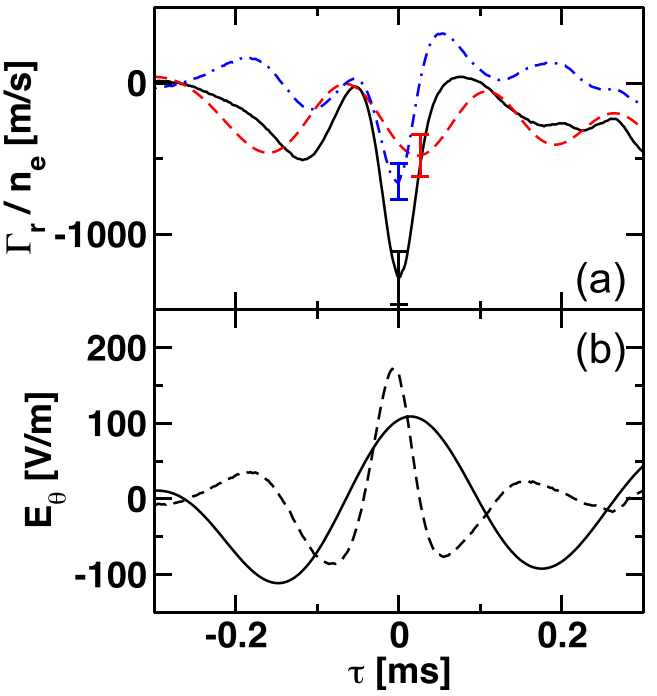

FIG. 6. (a) Lock-in averaged total particle flux (black solid), coherent particle flux (red dashed), and transient particle flux (blue dashed-dotted), normalized by the electron density. (b) Azimuthal electric field fluctuations in the coherent regime (solid) and the turbulence regime (dashed).

fluctuation as $\tilde{\phi}/\hat{\phi} > \tilde{n}_\mathrm{e}/\hat{n}_\mathrm{e}$. Considering the weighting by k_θ, i.e., $|E_\theta| = |k_\theta \phi|$, where k_θ is roughly proportional to the frequency, the third term is predicted to have a larger portion than the fourth term. In Fig. 6(a), error bars represent the standard deviation of the lock-in average. The coherent particle flux shows the slow time evolution, which seems to have an impact on the mean particle flux. In contrast, the transient particle flux involves the short time burst, making a pair of the positive and negative spikes that cancels contribution to the mean particle flux. Total particle flux hence only shows the single large negative spike, as the superimposition of $\Gamma_{r,\mathrm{coh}}$ and $\Gamma_{r,\mathrm{trans}}$. Figure 6(b) shows lock-in averaged time evolution of the azimuthal electric field fluctuation in the coherent regime $\hat{E}_\theta$ and the turbulence regime $\tilde{E}_\theta$, which are the difference between $\Gamma_{r,\mathrm{coh}} (\equiv \hat{n}_\mathrm{e}\hat{E}_\theta)$ and $\Gamma_{r,\mathrm{trans}} (\equiv \hat{n}_\mathrm{e}\tilde{E}_\theta)$. Indeed, the amplitude of $\tilde{E}_\theta$ exceeds that of $\hat{E}_\theta$ when the negative spike is seen in the total flux. If one takes the lock-in average with respect to the phase of the fundamental mode, the amplitude burst in $\tilde{E}_\theta$ does not appear. The large spike of the particle flux is caused by the irregular increase of the turbulence amplitude in the azimuthal electric field fluctuation. Dynamics that maintain the $\tilde{E}_\theta$ burst are clearly different from the period of the fundamental mode. A candidate could be a zonal flow at very low frequency (~0.3 kHz), as discussed in Refs. 27 and 35.

IV. DISCUSSION AND SUMMARY

In this article, we have discussed localization of a turbulence packet and its effect on intermittency of particle transport. According to the azimuthal correlation length of fluctuations, the fluctuation component was divided into

two different regimes, the coherent regime and the turbulence regime. The fluctuation in the coherent regime was considered to be the linearly excited D'Angelo mode (Kelvin-Helmholtz type instability driven by an axial velocity gradient). The fluctuation component in the turbulence regime was found to be azimuthally localized, at a phase of the global coherent modes. Distribution of squared bicoherence was computed, as an indicator of the nonlinear energy transfer function from the global coherent mode to the turbulence. Squared bicoherence was strong at a phase where the turbulence amplitude was large. As a result of the turbulence localization, the time evolution of radial particle flux became bursty. Statistical features such as skewness and kurtosis were strongly modified by the localized turbulence component, although contribution to the mean particle flux profile was small.

Global modes can modify turbulence properties by both linear and nonlinear processes. Similar phenomena could occur in fusion devices by the interaction of global modes and turbulence. This leads to quasi-coherent modes as observed in L-mode (LOC-SOC transitions TEXTOR/Tore Supra), H-mode (in EAST with DTEM perhaps the "KBMs" in DIII-D), and in I-mode (WCM–GAM is the global mode CMOD/ASDEX). Also, the interaction of global MHD modes and turbulence would be an example.

ACKNOWLEDGMENTS

We thank Professors K. Ida and S. Sakakibara for strong support. One of the authors (T.K.) acknowledges Dr. C. Moon for useful discussion and Mr. T. Mitsuzono for excellent operation of PANTA. This work was partly supported by the Grant-in-Aid for Scientific Research of JSPS (15H02155, 23244113, 26887047), the collaboration programs of RIAM of Kyushu University and NIFS, and Asada Science Foundation.

APPENDIX: DATA PROCESS METHODS

In order to capture periodic behavior of the plasma fluctuation measured at a single point, two kinds of average methods are used. Here, we consider that plasma dynamics is regulated with a periodic oscillation in plasma fluctuation, from which the basic period for conditional average is extracted. We propose two averaging techniques for the present analysis.

1. Lock-in average

When one observes a periodic signal with an oscilloscope, a trigger mode may be used to fix the position of the waveform at a point in the display. Lock-in average method provides an averaged time sequence by taking ensembles when a trigger condition is satisfied in the same way as the oscilloscope. The moment of trigger-on is defined as the origin of a new time series. In general, the trigger can be a combination of a reference signal and a threshold value. Here, we define the trigger-on as the time when a phase of a coherent oscillation passes over zero from negative to positive. For a signal $x(t)$, lock-in average is defined as

$$\bar{x}(\tau) = \frac{1}{N}\sum_{i=1}^{N} x(t_i + \tau), \tag{A1}$$

where $-T < \tau \le T$ and T is a specific time width. The value t_i indicates the i-th instance of trigger-on and N is the total number of the events. It should be noted that the lock-in average here is generally called conditional average, but here we use the present terminology in order to distinguish from the conditional average shown in the next subsection.

2. Conditional average for squared bicoherence

Squared bicoherence[36] is defined as

$$b^2(f_1,f_2) = \frac{|\langle X(t,f_1)X(t,f_2)X^*(t,f_3)\rangle|^2}{\langle |X(t,f_1)X(t,f_2)|^2\rangle\langle |X(t,f_3)|^2\rangle}, \tag{A2}$$

where $X(t,f)$ is time evolution of either the Fourier spectrum or the Wavelet spectrum of a signal $x(t)$, and frequency matching condition $f_3 = f_1 \pm f_2$ should hold. Asterisk represents the complex conjugate. Squared bicoherence expresses the degree of conservation of a phase relation among three waves as a value from 0 to 1. As is done frequently, by assuming stationarity of the time sequence, ensemble average has been substituted for the long duration average. In the situation in which there is a periodic variation of nonlinearity, that assumption is violated. Ensemble average should be performed within time windows where the nonlinearity can be regarded as identical. Because the nonlinearity varies periodically, the phase of a reference oscillation θ can be used to choose the windows for ensemble average. The phase is divided with a regular interval $\Delta\theta$, giving the range $(i-1)\Delta\theta < \theta \le i\Delta\theta$ for the i-th segment. For each segment, the squared bicoherence is computed using only the ensembles at which the phase is in the given range as

$$b_i^2(f_1,f_2) = \left.\frac{|\langle X(t,f_1)X(t,f_2)X^*(t,f_3)\rangle|^2}{\langle |X(t,f_1)X(t,f_2)|^2\rangle\langle |X(t,f_3)|^2\rangle}\right|_{(i-1)\Delta\theta<\theta\le i\Delta\theta}. \tag{A3}$$

The total number of the segment is given as $M = 2\pi/\Delta\theta$, where M should be an integer. Summed squared bicoherence is computed as

$$B_i^2(f_3) = \frac{1}{s}\sum_{f_1} b_i^2(f_1, f_3 - f_1), \tag{A4}$$

where s is the number of summands for each segment. This illustrates the intensity of nonlinear coupling between the fluctuation having f_3 and all the fluctuations satisfying the frequency matching conditions.

[1]Laurent, L., Plasma Phys. Controlled Fusion **28**, 85 (1986).
[2]Diamond, P. H., Itoh, S.-I., Itoh, K., and Hahm, T. S., Plasma Phys. Controlled Fusion **47**, R35 (2005).
[3]Fujisawa, A., Itoh, K., Iguchi, H., Matsuoka, K., Okamura, S., Shimizu, A., Minami, T., Yoshimura, Y., Nagaoka, K., Takahashi, C. *et al.*, Phys. Rev. Lett. **93**, 165002 (2004).
[4]Lin, Z., Hahm, T. S., Lee, W. W., Tang, W. M., and White, R. B., Science **281**, 1835–1837 (1998).

[5]Dif-Pradalier, G., Hornung, G., Ghendrih, P., Sarazin, Y., Clairet, F., Vermare, L., Diamond, P., Abiteboul, J., Cartier-Michaud, T., Ehrlacher, C., *et al*., Phys. Rev. Lett. **114**, 085004 (2015).
[6]Politzer, P. A., Phys. Rev. Lett. **84**, 1192 (2000).
[7]Beyer, P., Benkadda, S., Garbet, X., and Diamond, P., Phys. Rev. Lett. **85**, 4892 (2000).
[8]Inagaki, S., Tokuzawa, T., Itoh, K., Ida, K., Itoh, S.-I., Tamura, N., Sakakibara, S., Kasuya, N., Fujisawa, A., Kubo, S., *et al*., Phys. Rev. Lett. **107**, 115001 (2011).
[9]P. H. Diamond, S.-I. Itoh, and K. Itoh, *Modern Plasma Physics: Volume 1, Physical Kinetics of Turbulent Plasmas* (Cambridge University Press, 2010).
[10]Xu, Y., Hidalgo, C., Shesterikov, I., Berte, M., Dumortier, P., Van Schoor, M., Vergote, M., Krämer-Flecken, A., Koslowski, R., and Team, T., Nucl. Fusion **53**, 072001 (2013).
[11]Xu, M., Tynan, G., Diamond, P., Manz, P., Holland, C., Fedorczak, N., Thakur, S. C., Yu, J., Zhao, K., Dong, J., *et al*., Phys. Rev. Lett. **108**, 245001 (2012).
[12]Manz, P., Xu, M., Fedorczak, N., Thakur, S., and Tynan, G., Phys. Plasmas **19**, 012309 (2012).
[13]Nagashima, Y., Itoh, S.-I., Shinohara, S., Fukao, M., Fujisawa, A., Terasaka, K., Kawai, Y., Kasuya, N., Tynan, G. R., Diamond, P. H. *et al*., J. Phys. Soc. Jpn. **77**, 114501 (2008).
[14]Yamada, T., Itoh, S.-I., Inagaki, S., Nagashima, Y., Kasuya, N., Kamataki, K., Arakawa, H., Kobayashi, T., Yagi, M., Fujisawa, A. *et al*., Phys. Rev. Lett. **105**, 225002 (2010).
[15]Nagashima, Y., Itoh, S.-I., Inagaki, S., Oldenbürger, S., Kobayashi, T., Kawashima, K., Ohyama, N., Tobimatsu, Y., Yamada, S., and Yamashita, T., in *Proceedings of the 39th EPS Conference on Plasma Physics* (2012), P5.158.
[16]Nagashima, Y., Itoh, S.-I., Shinohara, S., Fukao, M., Fujisawa, A., Terasaka, K., Kawai, Y., Tynan, G. R., Diamond, P. H., Yagi, M., Inagaki, S., Yamada, T., and Itoh, K., Phys. Plasmas **16**, 020706 (2009).
[17]Yan, Z., Xu, M., Diamond, P., Holland, C., Müller, S., Tynan, G., and Yu, J., Phys. Rev. Lett. **104**, 065002 (2010).
[18]Inagaki, S., Kobayashi, T., Kosuga, Y., Itoh, S.-I., Mitsuzono, T., Nagashima, Y., Arakawa, H., Yamada, T., Miwa, Y., Kasuya, N., Sasaki, M., Lesur, M., Fujisawa, A., and Itoh, K., Sci. Rep. (submitted).
[19]Windisch, T., Grulke, O., and Klinger, T., Phys. Plasmas **13**, 122303 (2006).
[20]Antar, G., Yu, J., and Tynan, G., Phys. Plasma **14**, 022301 (2007).
[21]Ramisch, M., Greiner, F., Mahdizadeh, N., Rahbarnia, K., and Stroth, U., Plasma Phys. Controlled Fusion **49**, 777 (2007).
[22]Pace, D., Shi, M., Maggs, J., Morales, G., and Carter, T., Phys. Plasmas **15**, 122304 (2008).
[23]Manz, P., Xu, M., Müller, S., Fedorczak, N., Thakur, S., Yu, J., and Tynan, G., Phys. Rev. Lett. **107**, 195004 (2011).
[24]Cui, L., Tynan, G., Diamond, P., Thakur, S., and Brandt, C., Phys. Plasmas **22**, 050704 (2015).
[25]Shinohara, S., Hada, T., Motomura, T., Tanaka, K., Tanikawa, T., Toki, K., Tanaka, Y., and Shamrai, K. P., Phys. Plasmas **16**, 057104 (2009).
[26]Ignatenko, M., Azumi, M., Yagi, M., Shinohara, S., Itoh, S.-I., and Itoh, K., Jpn. J. Appl. Phys., Part 1 **46**, 1680 (2007).
[27]Arakawa, H., Kobayashi, T., Inagaki, S., Kasuya, N., Oldenbürger, S., Nagashima, Y., Yamada, T., Yagi, M., Fujisawa, A., Itoh, K., and Itoh, S.-I., Plasma Phys. Controlled Fusion **53**, 115009 (2011).
[28]Kobayashi, T., Inagaki, S., Arakawa, H., Oldenbüeger, S., Sasaki, M., Nagashima, Y., Yamada, T., Sugita, S., Yagi, M., Kasuya, N., Fujisawa, A., Itoh, S.-I., and Itoh, K., Plasma Fusion Res. **6**, 2401082 (2011).
[29]Kasuya, N., Yagi, M., Itoh, K., and Itoh, S.-I., Phys. Plasmas **15**, 052302 (2008).
[30]Yamada, T., Itoh, S.-I., Terasaka, K., Kasuya, N., Nagashima, Y., Shinohara, S., Maruta, T., Yagi, M., Inagaki, S., Kawai, Y., Fujisawa, A., and Itoh, K., Plasma Fusion Res. **3**, S1021 (2008).
[31]Yamada, T., Nagashima, Y., Inagaki, S., Kawai, Y., Yagi, M., Itoh, S.-I., Maruta, T., Shinohara, S., Terasaka, K., Kawaguchi, M. *et al*., Rev. Sci. Instrum. **78**, 123501 (2007).
[32]Manz, P., Xu, M., Thakur, S., and Tynan, G., Plasma Phys. Controlled Fusion **53**, 095001 (2011).
[33]Sasaki, M., Kasuya, N., Kobayashi, T., Arakawa, H., Itoh, K., Fukunaga, K., Yamada, T., Yagi, M., and Itoh, S.-I., Phys. Plasmas **22**, 032315 (2015).
[34]Kosuga, Y., Itoh, S.-I., and Itoh, K., Plasma Fusion Res. **10**, 3401024 (2015).
[35]Oldenbürger, S., Inagaki, S., Kobayashi, T., Arakawa, H., Ohyama, N., Kawashima, K., Tobimatsu, Y., Fujisawa, A., Itoh, K., and Itoh, S., Plasma Phys. Controlled Fusion **54**, 055002 (2012).
[36]Kim, Y. C. and Powers, E. J., IEEE Trans. Plasma Sci. **7**, 120–131 (1979).